

Probabilistic Human Mesh Recovery in 3D Scenes from Egocentric Views

Siwei Zhang¹ Qianli Ma^{1,3} Yan Zhang¹ Sadegh Aliakbarian² Darren Cosker² Siyu Tang¹
¹ETH Zürich ²Microsoft ³Max Planck Institute for Intelligent Systems
 {siwei.zhang, qianli.ma, yan.zhang, siyu.tang}@inf.ethz.ch
 {coskerdarren, saliakbarian}@microsoft.com

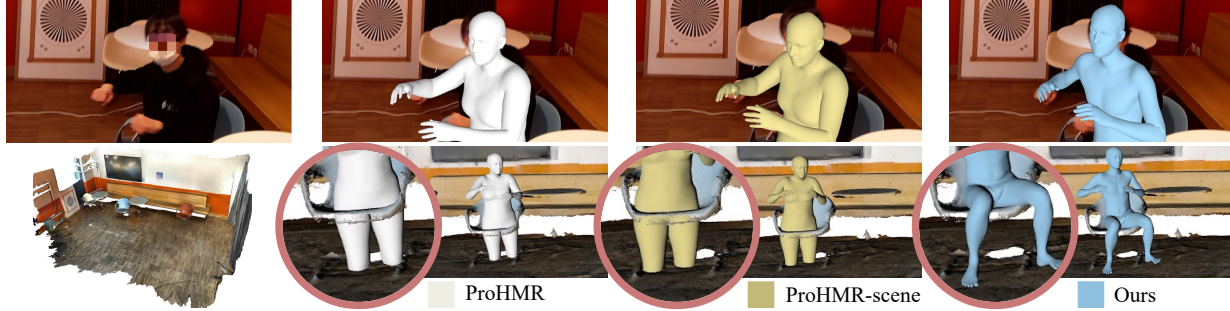


Figure 1: We propose EgoHMR, a novel scene-conditioned probabilistic method to recover the human mesh from an egocentric view image (typically with the body truncated) given the 3D environment. EgoHMR efficiently leverages the scene geometry and achieves significantly more plausible human-scene interactions compared to baseline methods, ProHMR [30] and the extended ProHMR-scene (Sec. 5.3), even with severe body truncations.

Abstract

Automatic perception of human behaviors during social interactions is crucial for AR/VR applications, and an essential component is estimation of plausible 3D human pose and shape of our social partners from the egocentric view. One of the biggest challenges of this task is severe body truncation due to close social distances in egocentric scenarios, which brings large pose ambiguities for unseen body parts. To tackle this challenge, we propose a novel scene-conditioned diffusion method to model the body pose distribution. Conditioned on the 3D scene geometry, the diffusion model generates bodies in plausible human-scene interactions, with the sampling guided by a physics-based collision score to further resolve human-scene interpenetrations. The classifier-free training enables flexible sampling with different conditions and enhanced diversity. A visibility-aware graph convolution model guided by per-joint visibility serves as the diffusion denoiser to incorporate inter-joint dependencies and per-body-part control. Extensive evaluations show that our method generates bodies in plausible interactions with 3D scenes, achieving both superior accuracy for visible joints and diversity for invisible body parts. The code will be available at <https://sanweiliti.github.io/egohmr/egohmr.html>.

1. Introduction

With the rapid development of Augmented and Virtual Reality (AR/VR) devices, understanding human actions, behaviors and interactions of our social partners (“interactee”) from the egocentric view is a vital component for head-mounted devices (HMDs) to truly become a virtual companion for humans. The first step towards the automatic perception of human behaviors and interactions for HMDs is to estimate 3D human pose and shape (*i.e.* human mesh recovery) of the interactee from egocentric view images.

The research community has extensively studied human mesh recovery from a single RGB image (usually captured with third-person view cameras) by predicting SMPL [37, 48] parameters from global image features [7, 22, 25, 28, 43]. However, their performance degrade significantly in egocentric images [74]. A major challenge presented in egocentric scenarios is frequent body truncation [36, 74], when individuals interact with each other within close proximity, while the HMD camera has a limited field-of-view. Since human poses are highly reliant on the surrounding environment, 3D scene structures can potentially provide strong cues to infer invisible body parts, which is crucial for precise understanding of human behaviors: sitting on a chair and standing on the ground may indicate distinct intentions and future behaviors. Following

PROX [13], we assume a rough 3D scene structure is available, as such information nowadays can be easily obtained with commodity sensors. Furthermore, visual localization and mapping, one of the extensively studied topics in computer vision, is progressing rapidly for head-mounted devices [50]. Therefore, we make the assumption that a coarse 3D model of the scene and the localization of the egocentric camera are readily available (*e.g.* in HoloLens2 [1]). In this paper, we focus on the challenging problem of estimating 3D human bodies that are heavily truncated from egocentric views due to the proximity between people and the motion of embodied cameras.

Given an egocentric image and the corresponding 3D environment, what should an ideal human mesh recovery method achieve? In contrast to previous studies that mostly pursue full-body pose accuracy, we argue the following properties are desired in the egocentric scenario: (1) natural and plausible human-scene interactions; (2) accurate body pose estimations consistent with image observations for visible joints; (3) a comprehensive conditional distribution to generate *diverse* and *plausible* poses for unobserved body parts. Several recent studies have attempted to tackle the problem of pose ambiguities caused by occlusions and body truncations. However, some methods can only produce a discrete number of body poses [3, 32, 46], ignoring the continuous nature of the pose manifold. Other approaches model the continuous body pose distribution via conditional variational autoencoder [51] or normalizing flows [30, 64], but with limited expressiveness. Furthermore, the 3D environment is often ignored although it provides strong cues for inferring missing body parts in the image.

To address these issues, we introduce EgoHMR, a novel scene-conditioned probabilistic approach, the first method to recover human mesh in 3D scenes from the egocentric view image. Inspired by the recent diffusion models that can generate high fidelity images [8, 15, 16, 55] and human motions [23, 39, 59, 66, 73] with flexible conditioning, our model is trained with a **conditional diffusion framework**, leveraging both the classifier-free guidance [16] and the classifier-guided diffusion sampling [8, 53, 56] for efficient scene conditioning. By training the model conditioning on a human-centric scene encoding, the diffusion denoiser can generate body poses with plausible human-scene interactions even with highly truncated bodies (see Fig. 1). The classifier-free training enables flexible sampling from models with or without image conditions, achieving accurate estimations of visible body parts while generating diverse plausible results for unseen body parts. On top of that, the diffusion sampling process is guided by the gradients of a **physics-based collision score guidance** in the classifier-guided sampling manner, which further resolves human-scene inter-penetrations without requiring additional time-consuming postprocessing.

To facilitate the learning of the multimodal distributions of the invisible body parts, we introduce a **visibility-aware graph convolution model** as the diffusion denoiser network, to explicitly guide the network to learn more expressive distribution for invisible body parts. Unlike existing methods [22, 30, 34, 64] that simply condition the full body pose on a global image feature, we condition the pose diffusion of each body joint on the joint visibility mask and the 3D scene feature, in addition to the image feature. With such explicit visibility guidance, the model learns to estimate accurate body pose for visible joints while encouraging diversity for truncated body parts. We adopt a graph convolution network (GCN) [24, 77] to better incorporate local dependencies between highly-relevant body parts (*e.g.* knee-foot) according to the human kinematic tree.

In summary, our contributions are: 1) a novel scene-conditioned diffusion model for probabilistic human mesh recovery in the 3D environment from egocentric images; 2) a physics-based collision score that guides the diffusion sampling process to further resolve human-scene inter-penetrations; 3) a visibility-aware GCN architecture that incorporates inter-joint dependencies for the pose diffusion, and enables per-body-part control via the per-joint visibility conditioning. With extensive evaluations, the proposed method demonstrates superior accuracy and diversity of generated human bodies from egocentric images, in natural and plausible interactions with the 3D environment.

2. Related Work

Human mesh recovery from a single image. Given a single RGB image, the task of deterministic 3D human mesh recovery has been widely studied in the literature, with regression-based methods [6, 7, 10, 22, 25, 26, 28, 29, 33–35, 43, 47, 58, 68, 72, 76], optimization-based methods [4, 9, 31, 48, 65] or hybrid methods [21, 27, 54], mostly adopting parametric 3D body models [4, 67] to represent the 3D human mesh. Most of recent regression-based methods train neural networks to regress SMPL [4] parameters from images [10, 22, 26, 34, 49]. Model-free methods [6, 7, 35, 43] regress human mesh vertices without relying on parametric body models. Optimization-based methods iteratively optimize the body model parameters to fit 2D keypoints, human silhouettes, *etc.* Some resort to self-contact [44], scene [13, 65] or object [57] constraints to model interactions. Hybrid methods seek to combine the strengths of both regression and optimization, for instance, SPIN [27], which integrates an optimization loop into the deep learning framework. However, these methods often lack robustness when dealing with truncated bodies, a typical challenge in egocentric scenarios, and cannot model the diverse nature of plausible missing body parts. 3D scene information is mostly disregarded, resulting in unrealistic human-scene interactions. In this work, we address

these challenges by proposing a scene-conditioned generative model for human mesh recovery in 3D scenes.

Multi-hypothesis for 3D human pose estimation. Due to the limited image observation and depth ambiguity, estimating 3D human pose from a single image can have multiple potential solutions, especially when body truncation is presented. Recent works seek to model this task as a generative process or predict multiple hypothesis of possible poses. A discrete number of hypotheses are generated in [3, 19, 32, 46]. To learn the continuous distribution of possible body poses, conditional variational autoencoders [51] or conditional normalizing flows [30, 64] are adopted to generate unlimited number of hypotheses, but relying on additional scoring functions for pose selection [51], or discriminators to stabilize the training [30, 64]. Nevertheless, the 3D scene constraint is usually not taken into account in this line of works. We leverage the diffusion process to model the inherent pose ambiguity, with flexible scene-conditioning strategies.

Egocentric human pose estimation. Most of existing works in egocentric human pose estimation targets the camera wearer’s 3D pose [12, 20, 38, 52, 60, 61, 70]. 3D pose estimation for a social partner from the egocentric view has been receiving growing attention [36, 45, 69]. However, the 3D scene geometry is neglected in [45, 69], while [36] employs the time-consuming optimization, without modelling the probabilistic distribution of unseen body parts.

Diffusion models for human motion/pose generation. Denoising Diffusion Models [15, 53, 55, 56] are becoming a popular choice for human motion generative models. Typically trained with the DDPM formulation [15] and based on Transformer-backbones, different methods vary on their choice of motion representation (e.g. skeletons [39, 73], joint rotations [2, 23, 62] or latent variables [66]) and downstream tasks. To generate plausible human-scene interactions, SceneDiffuser [17] condition the motion/pose diffusion model on 3D scenes and further guide the model with physics-based objectives at inference time. In a similar fashion, PhysDiff [71] incorporates a physics-based motion projection module in the inference loop to resolve typical flaws in motion synthesis such as foot-ground penetrations. While these methods all target human action *synthesis*, we take a different perspective and leverage Diffusion Models for a *perception* task — as a multi-proposal formulation to address the ambiguity in the egocentric pose estimation.

3. Preliminaries

SMPL body model [37]. We model the human mesh with the parametric SMPL body model. SMPL parametrizes a body as a function $\mathcal{M}_b(\gamma, \beta, \theta)$ of the global translation $\gamma \in \mathbb{R}^3$, body shape $\beta \in \mathbb{R}^{10}$, and full body pose $\theta \in \mathbb{R}^{24 \times 3}$ of 23 body joints, plus the global orientation, returning a mesh \mathcal{M}_b with 6890 vertices.

Conditional Diffusion Model. We use DDPM [15] as our formulation of pose diffusion model. DDPM learns a distribution of body poses θ through a forward diffusion process and an inverse denoising (sampling) process. The forward diffusion process is a Markov chain of added Gaussian noise over $t \in \{1, \dots, T\}$ steps:

$$q(\theta_t | \theta_{t-1}) = \mathcal{N}(\theta_t; \sqrt{\alpha_t} \theta_{t-1}, (1 - \alpha_t) \mathbf{I}), \quad (1)$$

where the variance $1 - \alpha_t \in (0, 1]$ increases with t according to a pre-defined schedule, and T is the total number of noise corruption steps.

At the core of the inverse process is a denoiser neural network $D(\cdot)$, which is trained to remove the added Gaussian noise based on condition signal c at each step t . Following the design of recent motion diffusion models [59], the denoiser predicts the clean signal itself: $\hat{\theta}_0 = D(\theta_t, t, c)$.

The Gaussian forward diffusion process has a special property that allows directly sampling θ_t from θ_0 :

$$\theta_t = \sqrt{\alpha_t} \theta_0 + \sqrt{1 - \alpha_t} \epsilon, \text{ where } \epsilon \sim \mathcal{N}(0, \mathbf{I}). \quad (2)$$

With this, training the denoiser amounts to sampling a random $t \in \{0, \dots, T - 1\}$, adding noise according to Eq. (2), and optimizing the *simple objective* [15]:

$$\mathcal{L}_{\text{simple}} = E_{\theta_0 \sim q(\theta_0 | c), t \sim [1, T]} [\|\theta_0 - D(\theta_t, t, c)\|_2^2]. \quad (3)$$

In this paper we use the subscript t to denote the diffusion timestep and superscript j for the body joint index.

4. Method

We introduce a novel scene-conditioned diffusion method to recover the human mesh in 3D environments from the egocentric image. Fig. 2 shows the overview of our model. Given an egocentric image \mathcal{I} with a truncated body, the camera intrinsics $\mathcal{K} = (f, c_x, c_y)$, and the 3D scene point cloud $\mathcal{S} \in \mathbb{R}^{N \times 3}$ with N points, our goal is to learn the conditional distribution of body poses $p(\theta | \mathcal{I}, \mathcal{S}, \mathcal{K})$, with the objective of generating humans that naturally interact with the scene while being aligned with the image observation. The body translation γ and shape β are learnt in a deterministic way following [30]. Here f and (c_x, c_y) denote the focal length and the camera center, respectively.

The diffusion denoising process (Sec. 3) is modeled by a visibility-aware graph convolution network (GCN), which achieves per-body-part control with the per-joint conditioning on the input image, scene geometry and joint visibility (Sec. 4.1). The diffusion model is trained in a classifier-free manner [16], enabling flexible sampling from both models that include or exclude image conditions to enhance diversity and expressiveness for truncated body parts. Guided by the gradients of a physics-based human-scene collision

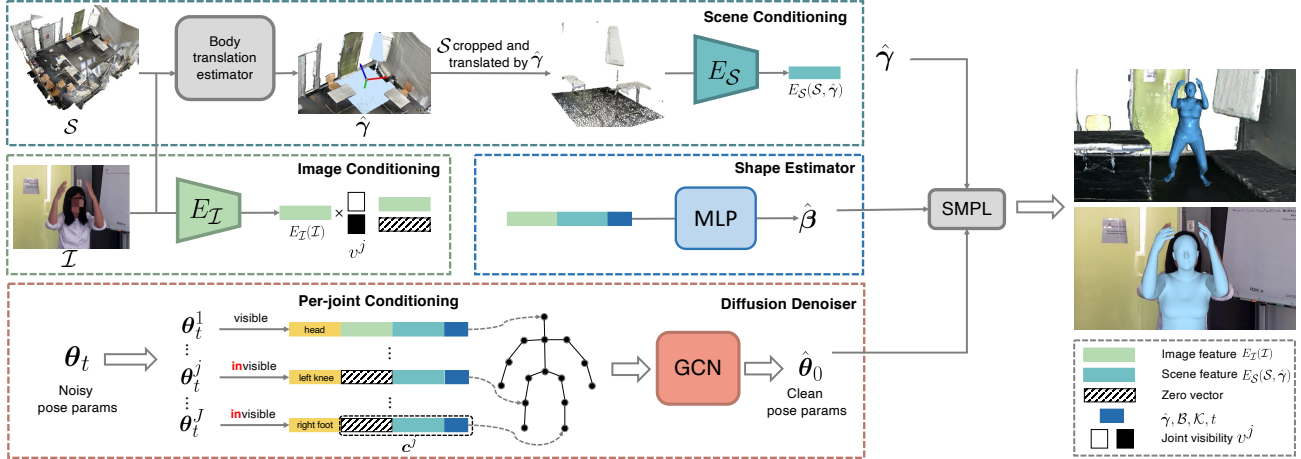


Figure 2: **Method overview.** Given an egocentric image \mathcal{I} containing a partially visible body and the 3D scene geometry \mathcal{S} , the proposed model generates a SMPL mesh with plausible human-scene interactions and conforming to the image observation. The model comprises a Scene Conditioning module to estimate the body translation $\hat{\gamma}$ and encode the local scene features, an Image Conditioning module to encode image features, a GCN-based Diffusion Denoiser to predict the clean body pose $\hat{\theta}_0$ from noisy pose θ_t with Per-joint Conditioning, and a Shape Estimator to estimate body shape $\hat{\beta}$.

score, we further resolve human-scene inter-penetrations during the diffusion sampling (Sec. 4.2). The training objectives are explained in Sec. 4.3.

4.1. Scene-conditioned Pose Diffusion Model

3D scene conditioning. To model fine-grained human-scene interactions, only a small region of the scene surrounding the human is relevant. An accurate global body translation provides better reasoning about local scene geometries, thus crucial for accurate and scene-plausible local body pose modelling. To this end, we propose a body translation estimator (see Fig. 2) to estimate the translation $\hat{\gamma}$ by extracting features from \mathcal{I} and the full 3D scene point cloud \mathcal{S} . The global scene features alleviate the scale ambiguity and localize the body in the 3D environment accurately (please refer to Supp. Mat. for more details). Given the estimated body translation $\hat{\gamma}$, scene vertices in a $2 \times 2m$ region around the human are selected and considered as the scene conditioning for the diffusion denoising process. Furthermore, the selected scene vertices are translated by $\hat{\gamma}$ such that the scene vertex origin is around the body pelvis. The translated scene point cloud is encoded by a scene encoder E_S into a localized human-centric scene feature $E_S(\mathcal{S}, \hat{\gamma})$ for modelling detailed interactions between the body and the 3D scene.

Per-joint conditioning. A ResNet50 backbone [14] E_I is used to encode the cropped input image I into a latent feature $E_I(\mathcal{I}) \in \mathbb{R}^{2048}$ as the image conditioning. However, regressing the full body pose directly from the global image feature as in previous works [22, 27, 30] loses the explicit joint visibility information. With the body truncated in the image, different properties are desired for different

body parts: the model should achieve pose accuracy for observed body joints, and pose expressiveness for truncated body parts. To achieve the per-body-part control, the 2D joint visibility mask $\mathcal{V} = (v^0, \dots, v^j, \dots, v^{J-1}) \in \mathbb{R}^J$ is extracted from the image via OpenPose [5] 2D joint detections, and passed to the diffusion model as the visibility condition. Here J denotes the joint number; and v^j equals to 1 if the j -th joint is visible in \mathcal{I} , otherwise 0.

Apart from above conditions, the bounding box information \mathcal{B} is additionally fed to the network inspired by [34], serving as a global-location-aware feature to better model global information:

$$\mathcal{B} = (b_x, b_y, b) / f, \quad (4)$$

where b_x, b_y, b denote the bounding box center coordinates and bounding box size in the full image, respectively. The full condition c^j for j -th joint is formulated as the concatenation of: the image feature (masked out by v^j if the joint is not visible), 3D scene feature, estimated body translation, bounding box feature, camera intrinsics and the diffusion timestep t :

$$c^j = (E_I(\mathcal{I}) \cdot v^j, E_S(\mathcal{S}, \hat{\gamma}), \hat{\gamma}, \mathcal{B}, \mathcal{K}, t). \quad (5)$$

By conditioning on a per-joint basis, the model achieves flexible control over each body part according to the joint visibility. This allows for both accurate pose estimation of visible body parts, and flexibility for invisible body parts.

Diffusion denoiser architecture. At diffusion timestep t , for the noisy body pose parameters θ_t , the diffusion denoiser D predicts the clean pose parameter $\hat{\theta}_0$ conditioned on c . Previous works either use a single MLP for the full

body pose [22, 30, 34, 64] with redundant dependencies between irrelevant joints, or employ a separate MLP for each joint [25] which fully ignores joint dependencies. Instead, we adopt a graph convolution network (GCN) [24, 77] as the denoising function D . Given the predefined human kinematic tree, GCN models inter-joint dependencies by treating the human skeleton as a graph, where each node corresponds to a body joint. Specifically, for each joint j , the noisy pose parameters θ_t^j is embedded and concatenated with the per-joint conditioning c^j as the feature for node j in the GCN (see Fig. 2). We adopt the modulated GCN [77] for the implementation. Different from vanilla GCN [24], the modulated GCN learns node-specific modulation vectors to disentangle joint feature transformations, such that different relations can be learnt between joints. It also modulates the affinity matrix with learnable parameters to model additional edges beyond the human skeleton [77]. Please refer to Supp. Mat. for implementation details.

Shape estimator. As the body shape β is a global feature and more robust to body truncations, an MLP branch (the body shape estimator in Fig. 2) predicts $\hat{\beta}$ from the conditions $(E_X(\mathcal{I}), E_S(\mathcal{S}, \hat{\gamma}), \hat{\gamma}, \mathcal{B}, \mathcal{K})$ in a deterministic way.

4.2. Scene-guided Sampling

We use the DDPM [15] sampler at inference time. At each sampling step t , the denoiser predicts $\hat{\theta}_0 = D(\theta_t, t, c)$, which is noised back to θ_{t-1} by sampling from the Gaussian distribution:

$$\theta_{t-1} \sim \mathcal{N}(\mu_t(\theta_t, \hat{\theta}_0), \Sigma_t), \quad (6)$$

where $\mu_t(\theta_t, \hat{\theta}_0)$ is a linear combination of θ_t and $\hat{\theta}_0$, and Σ_t is a scheduled Gaussian distribution as in [15]. The sampling is iteratively repeated from $t = T - 1$ until $t = 0$.

Classifier-free guidance. The diffusion model D is trained with classifier-free guidance [16] by randomly masking out the image feature $E_X(\mathcal{I})$ for all joints with a probability of 5% during training, such that the model also learns the pose distribution independent from the image, enabling flexible sampling. By combining the poses of visible joints sampled from the full-conditioned model and the poses of invisible joints sampled from the model excluding image conditions:

$$\hat{\theta}_0 = D(\theta_t, t, c) \odot \mathcal{V} + D(\theta_t, t, c_\phi) \odot (1 - \mathcal{V}), \quad (7)$$

we achieve better per-body-part control, with enhanced diversity for invisible body parts while maintaining the accuracy of visible body parts (see Sec. 5.5 for the ablation study). Here \odot denotes multiplying the joint visibility mask with the pose of each joint, and c_ϕ is the condition excluding image features.

Collision score guided sampling. The proposed scene encoding in Sec. 4.1 implicitly incorporates the 3D environment constraint into the diffusion conditioning. However,

the network cannot fully resolve the human-scene collisions in a fine-grained way. Another way to incorporate conditions into the diffusion model is the score-function based guidance. As shown in previous works [8, 53, 56], a pre-trained classifier can be adopted to provide class information by adding the gradients of the classifier at each sampling step to the diffusion model, to guide the sampling process towards the class label. Inspired by this, we propose a collision score guided sampling strategy to further resolve implausible human-scene inter-penetrations, by leveraging implicit body representations [41, 42]. We use COAP [41] to model neural articulated occupancy of human bodies as the zero-level set $f_\Theta(q|\mathcal{G}) = 0$, where q is the input query point and $\mathcal{G}(\theta, \beta)$ is the input bone transformations. By querying each scene vertex near the body to see if it is inside of the human volume, the collision score is defined as:

$$\mathcal{J}(\theta) = \frac{1}{|\mathcal{S}|} \sum_{q \in \mathcal{S}} \sigma(f_\Theta(q|\mathcal{G})) \mathbb{1}_{f_\Theta(q|\mathcal{G}) > 0}, \quad (8)$$

where $\sigma(\cdot)$ stands for the sigmoid function. The gradient $\nabla \mathcal{J}(\theta)$ efficiently guides the diffusion sampling process to further alleviate the human-scene collisions (see Sec. 5.5 for the ablation study) by modifying Eq. (6) to:

$$\theta_{t-1} \sim \mathcal{N}(\mu_t(\theta_t, \hat{\theta}_0) + a \Sigma_t \nabla \mathcal{J}(\theta_t), \Sigma_t), \quad (9)$$

where the guidance is modulated by Σ_t and a scale factor a .

4.3. Training Objectives

The diffusion model is trained with $\mathcal{L}_{\text{simple}}$ in Eq. (3) for body pose $\hat{\theta}_0$, together with the the 3D joint loss \mathcal{L}_{3D} , the 2D keypoint re-projection loss \mathcal{L}_{2D} calculated in the full image frame, and the shape loss \mathcal{L}_β :

$$\begin{aligned} \mathcal{L}_{3D} &= \|FK(\hat{\theta}_0, \hat{\beta}) - FK(\theta_0, \beta)\|^2, \\ \mathcal{L}_{2D} &= \|\Pi_{\mathcal{K}}(J_{3D} + \hat{\gamma}) - J_{\text{est}}\|^2, \\ \mathcal{L}_\beta &= \|\hat{\beta} - \beta\|^2. \end{aligned} \quad (10)$$

Here $FK(\cdot)$ denotes the SMPL joint regressor to obtain 3D joint coordinates. J_{est} is the 2D body keypoint detections, and $\Pi_{\mathcal{K}}$ denotes the 3D to 2D projection in the full image with camera intrinsics \mathcal{K} . The overall loss is defined as:

$$\begin{aligned} \mathcal{L} &= \mathcal{L}_{\text{simple}} + \lambda_{3D} \mathcal{L}_{3D} + \lambda_{2D} \mathcal{L}_{2D} + \lambda_\beta \mathcal{L}_\beta \\ &\quad + \lambda_{\text{coll}} \mathcal{L}_{\text{coll}} + \lambda_{\text{orth}} \mathcal{L}_{\text{orth}}, \end{aligned} \quad (11)$$

where $\mathcal{L}_{\text{orth}}$ is a regularizer to force the generated 6D pose rotation representation to be orthonormal, $\mathcal{L}_{\text{coll}}$ is the scene collision loss the same as defined in Eq. (8), and λ_s are the corresponding weight factors for each loss term.

5. Experiments

5.1. Dataset

Most of existing datasets for 3D human pose evaluation are either captured from the third-person view with the full

body visible [13, 18, 40, 63], or do not contain the 3D environment [45]. The most relevant dataset is **EgoBody** [74], a large-scale egocentric dataset capturing 3D human motions during social interactions in 3D scenes. Each sequence involves two people interacting with each other in 3D environments, and one subject wears a head-mounted camera to capture the egocentric images containing the other *interactee*. Due to the close social interaction distance, the captured egocentric images typically exhibit strong body truncations for the interactee. We use the official train / test splits for training and evaluation, which include 90,120 / 62,140 frames, respectively.

5.2. Evaluation Metrics

Strong body truncations pose inherent ambiguity for invisible body parts, while the visible body parts are relatively deterministic given the image observations, thus evaluating the accuracy of full body joints together as in [3, 30] is not suitable for such tasks. We propose to evaluate the proposed method from the following aspects.

Accuracy. We employ the common metrics: Mean Per-Joint Position Error (MPJPE) and Vertex-to-Vertex (V2V) errors in *mm* to evaluate the accuracy of estimated body pose and shape. For MPJPE, we report different variations: G-MPJPE as the joint error in the global coordinate; MPJPE as the pelvis-aligned joint errors, and PA-MPJPE as the joint errors after Procrustes Alignment [11]. We report mean MPJPE and V2V metrics over n samples for visible joints. Nevertheless, such evaluation protocol assumes a single correct ground truth prediction, which does not hold for invisible joints. Instead of the mean error, we report *min-of-n* MPJPE for invisible body parts following [3]. To be specific, among the generated n samples for each input image, we select the one with the minimum MPJPE for all evaluated methods.

Physical plausibility. We evaluate the collision and contact scores between the body mesh and the 3D scene. As the clean scene signed distance field (SDF) is not available in EgoBody, we define the collision score as the ratio of the number of scene vertices inside of the body mesh to the number of all scene vertices. Note that the absolute scale of the collision score may vary with different size of the 3D scene, but within the same scene surface, the relative comparison between different methods indicates different collision levels. We use the cropped scene as described in Sec. 4.1 for evaluation (with a fixed size of 20,000 vertices). Following [17], the contact score is defined as 1 if the body contacts with the scene in a distance within a threshold (2 *cm*), otherwise 0. We report the mean collision score and contact score over all test samples. Note that a model with better physical plausibility should achieve *both* a lower collision score and a higher contact score.

Diversity. Diversity is evaluated for invisible body parts

to demonstrate the expressiveness of the methods, by calculating the standard deviation (std) and Average Pairwise Distance (APD) of invisible body joints [17]. A higher diversity is desired, yet there is usually a *trade-off* between diversity and accuracy/plausibility. An ideal model should predict diverse poses for invisible body parts, with accurate visible body poses and plausible human-scene interactions.

5.3. Baselines and Our Method

As there is no existing work for our task, we compare our method with the following baselines: (1) ProHMR [30], the state-of-the-art method for probabilistic human mesh recovery from a single image based on conditional normalizing flows; (2) ProHMR-scene, in which we enhance the ProHMR framework by incorporating the scene geometry \mathcal{S} with a global scene feature encoder.

The ProHMR framework is trained with 2D and 3D supervisions for the sample drawn from $z = 0$ (referred as the ‘mode’), such that the ‘mode’ can be used as a predictive model (see [30] for details). Different training weights for the samples drawn from $z \neq 0$ yields a trade-off between the accuracy and diversity for the generated multiple hypotheses. Here z denotes the latent space of the normalizing flow. To demonstrate this trade-off, we train the ProHMR-scene baseline with different training configurations. For samples drawn from $z \neq 0$, we supervise with: 1) only 2D re-projection loss (the same as in [30]), denoted as *-orig*; 2) 3D supervision with small weights, denoted as *-weak-3D*; 3) 3D supervision with large weights, denoted as *-strong-3D*. Here the 3D supervision refers to the loss on 3D body joints and SMPL parameters. Please refer to Supp. Mat. for details of the baseline models.

5.4. Results

Tab. 1 shows the quantitative results. Compared to the baselines, our method achieves the best G-MPJPE, MPJPE and V2V metrics for visible joints, demonstrating accurate estimations of the global translation, local body pose for visible joints and body shape. For truncated body joints, our method obtains the best *min-of-n* MPJPE, indicating that our generated results better covers the ground truth distribution for truncated body parts than baselines, thanks to the efficient scene conditioning. Our method also outperforms the baselines with the higher contact ratios and significantly better collision scores. In particular, our collision score decreased **45%** compared with ProHMR, and **37%** compared with the best ProHMR-scene model. This indicates that the proposed method can effectively leverage the scene conditions and resolve body-scene inter-penetrations, while achieving better contact relations between the body and the 3D environment. Fig. 3 (left) shows the qualitative results and the comparison with the baseline method.

From the results among different ProHMR-scene base-

Table 1: **Evaluation for accuracy, physical plausibility and diversity on EgoBody.** Here *-vis* and *-invis* denote visible and invisible joints, respectively. ‘coll’ and ‘contact’ refer to the collision and contact scores, respectively. The percentage for the collision score denotes how much improvement the corresponding method has achieved compared with the ProHMR baseline. The best results are in boldface.

n	Method	G-MPJPE ↓ <i>-vis</i>	MPJPE ↓ <i>-vis</i>	PA-MPJPE ↓ <i>-vis</i>	V2V ↓ <i>-vis</i>	<i>min-of-n</i> MPJPE ↓ <i>-invis</i>	coll ↓	contact ↑	std ↑ <i>-invis</i>	APD ↑ <i>-invis</i>
5	ProHMR [30]	181.33	72.92	46.57	90.88	128.56	0.00346 (-)	0.94	26.53	32.95
	ProHMR-scene-orig	133.72	73.13	48.87	91.59	117.88	0.00305 (12%)	0.96	35.42	44.02
	Ours	128.62	65.70	47.17	82.93	107.77	0.00191 (45%)	0.99	29.59	35.15
10	ProHMR [30]	181.70	73.65	47.06	91.84	121.67	0.00346 (-)	0.94	29.26	35.06
	ProHMR-scene-orig	134.57	74.42	49.63	93.21	110.64	0.00305 (12%)	0.96	39.07	46.86
	Ours	128.60	65.69	47.20	82.94	100.75	0.00191 (45%)	0.99	29.59	35.15
20	ProHMR [30]	181.87	73.99	47.29	92.28	115.48	0.00346 (-)	0.93	30.55	36.14
	ProHMR-scene-orig	134.97	75.03	49.98	93.98	103.81	0.00306 (12%)	0.96	40.82	48.32
	ProHMR-scene-weak-3D	131.51	67.81	46.94	85.05	111.68	0.00313 (10%)	0.96	21.79	25.67
	ProHMR-scene-strong-3D	134.40	66.42	45.96	82.99	123.34	0.00316 (9%)	0.97	13.01	15.23
	Ours	128.60	65.69	47.19	82.94	94.96	0.00191(45%)	0.99	30.23	35.14



Figure 3: **Qualitative results on EgoBody dataset.** The left part shows the comparison between the baseline methods and our proposed method. The right part demonstrates the effectiveness of our proposed scene collision score guidance \mathcal{J}_θ to further resolve human-scene inter-penetrations. Red circles point to human-scene collisions.

Table 2: **Ablation study.** \mathcal{J}_θ and CF denote the collision score guidance and classifier-free guidance during the diffusion sampling (Sec 4.2). $\mathcal{L}_{\text{coll}}$ denotes the collision loss for training (Eq. (11)). All results are reported for $n = 20$.

Method	MPJPE ↓ -vis	<i>min-of-n</i> MPJPE ↓ -invis	coll ↓	contact ↑	std ↑ -invis	APD ↑ -invis
Ours	65.69	94.96	0.00191	0.99	30.23	35.14
Ours w/o \mathcal{J}_θ	65.09	97.20	0.00225	0.99	21.53	25.32
Ours w/o \mathcal{J}_θ w/o CF	64.58	98.82	0.00229	0.99	15.75	19.56
Ours w/o \mathcal{J}_θ w/o CF w/o $\mathcal{L}_{\text{coll}}$	64.91	96.26	0.00302	0.99	22.94	21.79



Figure 4: **Multiple samples.** Given the same input, our method can generate diverse poses for invisible body parts.

lines ($n = 20$) in Tab. 1, we can clearly see a trade-off between the accuracy and diversity: stronger 3D supervision (ProHMR-scene-*strong-3D*) has better accuracy for visible body parts (MPJPE-*vis*), yet lower diversity (std-*invis* and APD-*invis*) for invisible joints. The reason behind this is that the ProHMR framework, like many other existing works, condition the generative process of full body pose only on the global image feature. In contrast, our method leverages the joint visibility and the GCN architecture, achieving the best MPJPE for visible joints, diverse poses for invisible joints, and natural human-scene interactions (see Fig. 4), while the baseline with a similar diversity level (ProHMR) and the baseline with the highest diversity (ProHMR-scene-*orig*) exhibit much higher MPJPE errors and more severe human-scene collisions. There is a very slight increase for PA-MPJPE of our model compared to the ProHMR-scene-*strong/weak-3D* baselines, while we obtain a much higher diversity for invisible body joints. This reveals that our method achieves flexible per-body-part control to balance between the accuracy and diversity for different body parts.

5.5. Ablation Study

To investigate the influences of different training and sampling schemes for the diffusion model, we perform an ablation study and the results are shown in Tab. 2. The scene collision score efficiently resolves the human-scene interpenetrations from two different perspectives: via the collision loss $\mathcal{L}_{\text{coll}}$ during training and via the explicit collision score guidance \mathcal{J}_θ during the diffusion sampling (Eq. (9)). Fig. 3 (right) shows that the collision score guidance \mathcal{J}_θ improves the human-scene interaction relationships. The classifier-free guidance during the diffusion sampling in

Eq. (7) significantly improves the sample diversity, by leveraging the invisible joints sampled from the model trained excluding the image conditions. It is worth mentioning that the collision score guidance \mathcal{J}_θ also contributes to the sample diversity. This is not surprising as the gradients of \mathcal{J}_θ can potentially optimize the body pose to different directions given different initial body poses.

Compared with the trade-off in the ProHMR-based methods where the accuracy sacrifices a lot for diversity (and vice versa), the classifier-free guidance and the collision score guidance in our model only bring marginal changes for the MPJPE of visible body parts, in the trade-off for significantly enhanced physical plausibility, sample diversity and better *min-of-n* MPJPE for unobserved joints.

6. Conclusion

This paper introduces a novel scene-conditioned probabilistic approach for human mesh recovery from the egocentric image given the 3D scene geometry. The proposed diffusion model efficiently leverages the scene conditions and joint visibility to achieve per-body-part control and model human-scene interactions. The classifier-free guidance and the collision score guidance enables flexible sampling process with further enhanced diversity and physical plausibility. We demonstrate that our model generates human bodies in realistic interactions with the 3D environment, with diverse poses for invisible body parts while conforming to the image observation. Nevertheless, the current method also has limitations. For example, currently only a single frame is considered as the input. A promising future direction is to further exploit temporal information to reconstruct temporally consistent human motions from the egocentric view.

Acknowledgements. This work was supported by Microsoft Mixed Reality & AI Zurich Lab PhD scholarship. Qianli Ma is partially funded by the Max Planck ETH Center for Learning Systems. We sincerely thank Korrawe Karunratanakul, Marko Mihajlovic and Shaofei Wang for the fruitful discussions.

References

- [1] Microsoft Hololens2. <https://www.microsoft.com/en-us/hololens>. 2
- [2] Simon Alexander, Rajmund Nagy, Jonas Beskow, and Gustav Eje Henter. Listen, denoise, action! audio-driven motion synthesis with diffusion models. *arXiv preprint arXiv:2211.09707*, 2022. 3
- [3] Benjamin Biggs, David Novotny, Sebastien Ehrhardt, Hanbyul Joo, Ben Graham, and Andrea Vedaldi. 3d multi-bodies: Fitting sets of plausible 3d human models to ambiguous image data. *Advances in Neural Information Processing Systems*, 33:20496–20507, 2020. 2, 3, 6
- [4] Federica Bogo, Angjoo Kanazawa, Christoph Lassner, Peter Gehler, Javier Romero, and Michael J. Black. Keep it SMPL: Automatic estimation of 3D human pose and shape from a single image. In *European Conference on Computer Vision*, pages 561–578, 2016. 2
- [5] Z. Cao, G. Hidalgo Martinez, T. Simon, S. Wei, and Y. A. Sheikh. Openpose: Realtime multi-person 2d pose estimation using part affinity fields. *IEEE Transactions on Pattern Analysis and Machine Intelligence*, 2019. 4
- [6] Junhyeong Cho, Kim Youwang, and Tae-Hyun Oh. Cross-attention of disentangled modalities for 3D human mesh recovery with transformers. In *Computer Vision–ECCV 2022: 17th European Conference, Tel Aviv, Israel, October 23–27, 2022, Proceedings, Part I*, pages 342–359. Springer, 2022. 2
- [7] Hongsuk Choi, Gyeongseok Moon, and Kyoung Mu Lee. Pose2mesh: Graph convolutional network for 3D human pose and mesh recovery from a 2D human pose. In *European Conference on Computer Vision (ECCV)*, 2020. 1, 2
- [8] Prafulla Dhariwal and Alexander Nichol. Diffusion models beat gans on image synthesis. *Advances in Neural Information Processing Systems*, 34:8780–8794, 2021. 2, 5
- [9] Qi Fang, Qing Shuai, Junting Dong, Hujun Bao, and Xiaowei Zhou. Reconstructing 3D human pose by watching humans in the mirror. In *Proceedings of the IEEE/CVF Conference on Computer Vision and Pattern Recognition*, pages 12814–12823, 2021. 2
- [10] Georgios Georgakis, Ren Li, Srikrishna Karanam, Terrence Chen, Jana Košecá, and Ziyang Wu. Hierarchical kinematic human mesh recovery. In *Computer Vision–ECCV 2020: 16th European Conference, Glasgow, UK, August 23–28, 2020, Proceedings, Part XVII 16*, pages 768–784. Springer, 2020. 2
- [11] John C Gower. Generalized procrustes analysis. *Psychometrika*, 40(1):33–51, 1975. 6
- [12] Vladimir Guzov, Aymen Mir, Torsten Sattler, and Gerard Pons-Moll. Human positioning system (hps): 3d human pose estimation and self-localization in large scenes from body-mounted sensors. In *Proceedings of the IEEE/CVF Conference on Computer Vision and Pattern Recognition*, pages 4318–4329, 2021. 3
- [13] Mohamed Hassan, Vasileios Choutas, Dimitrios Tzionas, and Michael J Black. Resolving 3D human pose ambiguities with 3D scene constraints. In *Proceedings of the IEEE/CVF international conference on computer vision*, pages 2282–2292, 2019. 2, 6
- [14] Kaiming He, Xiangyu Zhang, Shaoqing Ren, and Jian Sun. Deep residual learning for image recognition. In *Proceedings of the IEEE conference on computer vision and pattern recognition*, pages 770–778, 2016. 4, 2
- [15] Jonathan Ho, Ajay Jain, and Pieter Abbeel. Denoising diffusion probabilistic models. *Advances in Neural Information Processing Systems*, 33:6840–6851, 2020. 2, 3, 5
- [16] Jonathan Ho and Tim Salimans. Classifier-free diffusion guidance. *NeurIPS 2021 Workshop on Deep Generative Models and Downstream Applications*, 2021. 2, 3, 5
- [17] Siyuan Huang, Zan Wang, Puhao Li, Baoxiong Jia, Tengyu Liu, Yixin Zhu, Wei Liang, and Song-Chun Zhu. Diffusion-based generation, optimization, and planning in 3d scenes. *arXiv preprint arXiv:2301.06015*, 2023. 3, 6
- [18] Catalin Ionescu, Dragos Papava, Vlad Olaru, and Cristian Sminchisescu. Human3.6m: Large scale datasets and predictive methods for 3d human sensing in natural environments. *IEEE transactions on pattern analysis and machine intelligence*, 36(7):1325–1339, 2013. 6
- [19] Ehsan Jahangiri and Alan L Yuille. Generating multiple diverse hypotheses for human 3D pose consistent with 2D joint detections. In *Proceedings of the IEEE International Conference on Computer Vision Workshops*, pages 805–814, 2017. 3
- [20] Hao Jiang and Kristen Grauman. Seeing invisible poses: Estimating 3d body pose from egocentric video. In *2017 IEEE Conference on Computer Vision and Pattern Recognition (CVPR)*, pages 3501–3509. IEEE, 2017. 3
- [21] Hanbyul Joo, Natalia Neverova, and Andrea Vedaldi. Exemplar fine-tuning for 3D human pose fitting towards in-the-wild 3D human pose estimation. 2021. 2
- [22] Angjoo Kanazawa, Michael J Black, David W Jacobs, and Jitendra Malik. End-to-end recovery of human shape and pose. In *Proceedings of the IEEE Conference on Computer Vision and Pattern Recognition*, pages 7122–7131, 2018. 1, 2, 4, 5
- [23] Jihoon Kim, Jiseob Kim, and Sungjoon Choi. Flame: Free-form language-based motion synthesis & editing. *arXiv preprint arXiv:2209.00349*, 2022. 2, 3
- [24] Thomas N. Kipf and Max Welling. Semi-supervised classification with graph convolutional networks. In *5th International Conference on Learning Representations, ICLR 2017, Toulon, France, April 24–26, 2017, Conference Track Proceedings*, 2017. 2, 5
- [25] Muhammed Kocabas, Chun-Hao P. Huang, Otmar Hilliges, and Michael J. Black. PARE: Part attention regressor for 3D human body estimation. In *Proceedings International Conference on Computer Vision (ICCV)*, pages 11127–11137. IEEE, Oct. 2021. 1, 2, 5
- [26] Muhammed Kocabas, Chun-Hao P. Huang, Joachim Tesch, Lea Müller, Otmar Hilliges, and Michael J. Black. SPEC: Seeing people in the wild with an estimated camera. In *Proc. International Conference on Computer Vision (ICCV)*, pages

- 11035–11045, Oct. 2021. 2
- [27] Nikos Kolotouros, Georgios Pavlakos, Michael J Black, and Kostas Daniilidis. Learning to reconstruct 3D human pose and shape via model-fitting in the loop. In *Proceedings of the IEEE International Conference on Computer Vision*, pages 2252–2261, 2019. 2, 4
- [28] Nikos Kolotouros, Georgios Pavlakos, and Kostas Daniilidis. Convolutional mesh regression for single-image human shape reconstruction. In *CVPR*, 2019. 1, 2
- [29] Nikos Kolotouros, Georgios Pavlakos, and Kostas Daniilidis. Convolutional mesh regression for single-image human shape reconstruction. In *Proceedings of the IEEE/CVF Conference on Computer Vision and Pattern Recognition*, pages 4501–4510, 2019. 2
- [30] Nikos Kolotouros, Georgios Pavlakos, Dinesh Jayaraman, and Kostas Daniilidis. Probabilistic modeling for human mesh recovery. In *Proceedings of the IEEE/CVF international conference on computer vision*, pages 11605–11614, 2021. 1, 2, 3, 4, 5, 6, 7
- [31] Christoph Lassner, Javier Romero, Martin Kiefel, Federica Bogo, Michael J Black, and Peter V Gehler. Unite the people: Closing the loop between 3D and 2D human representations. In *Proceedings of the IEEE conference on computer vision and pattern recognition*, pages 6050–6059, 2017. 2
- [32] Chen Li and Gim Hee Lee. Generating multiple hypotheses for 3D human pose estimation with mixture density network. In *Proceedings of the IEEE/CVF conference on computer vision and pattern recognition*, pages 9887–9895, 2019. 2, 3
- [33] Jiefeng Li, Chao Xu, Zhicun Chen, Siyuan Bian, Lixin Yang, and Cewu Lu. Hybrik: A hybrid analytical-neural inverse kinematics solution for 3D human pose and shape estimation. In *Proceedings of the IEEE/CVF Conference on Computer Vision and Pattern Recognition*, pages 3383–3393, 2021. 2
- [34] Zhihao Li, Jianzhuang Liu, Zhensong Zhang, Songcen Xu, and Youliang Yan. CLIFF: Carrying location information in full frames into human pose and shape estimation. In *Computer Vision—ECCV 2022: 17th European Conference, Tel Aviv, Israel, October 23–27, 2022, Proceedings, Part V*, pages 590–606. Springer, 2022. 2, 4, 5
- [35] Kevin Lin, Lijuan Wang, and Zicheng Liu. End-to-end human pose and mesh reconstruction with transformers. In *CVPR*, 2021. 2
- [36] Miao Liu, Dexin Yang, Yan Zhang, Zhaopeng Cui, James M Rehg, and Siyu Tang. 4d human body capture from egocentric video via 3d scene grounding. In *2021 International Conference on 3D Vision (3DV)*, pages 930–939. IEEE, 2021. 1, 3
- [37] Matthew Loper, Naureen Mahmood, Javier Romero, Gerard Pons-Moll, and Michael J Black. SMPL: A skinned multi-person linear model. *ACM Trans. Gr.*, 34(6):248, 2015. 1, 3
- [38] Zhengyi Luo, Ryo Hachiuma, Ye Yuan, Shun Iwase, and Kris M Kitani. Kinematics-guided reinforcement learning for object-aware 3d ego-pose estimation. *arXiv preprint arXiv:2011.04837*, 2020. 3
- [39] Jianxin Ma, Shuai Bai, and Chang Zhou. Pretrained diffusion models for unified human motion synthesis. *arXiv preprint arXiv:2212.02837*, 2022. 2, 3
- [40] Dushyant Mehta, Helge Rhodin, Dan Casas, Pascal Fua, Oleksandr Sotnychenko, Weipeng Xu, and Christian Theobalt. Monocular 3d human pose estimation in the wild using improved cnn supervision. In *3D Vision (3DV), 2017 Fifth International Conference on*. IEEE, 2017. 6
- [41] Marko Mihajlovic, Shunsuke Saito, Aayush Bansal, Michael Zollhoefer, and Siyu Tang. Coap: Compositional articulated occupancy of people. In *Proceedings of the IEEE/CVF Conference on Computer Vision and Pattern Recognition*, pages 13201–13210, 2022. 5
- [42] Marko Mihajlovic, Yan Zhang, Michael J Black, and Siyu Tang. LEAP: Learning articulated occupancy of people. In *Proceedings IEEE Conf. on Computer Vision and Pattern Recognition (CVPR)*, June 2021. 5
- [43] Gyeongsik Moon and Kyoung Mu Lee. I2l-meshnet: Image-to-lixel prediction network for accurate 3D human pose and mesh estimation from a single RGB image. In *European Conference on Computer Vision (ECCV)*, 2020. 1, 2
- [44] Lea Muller, Ahmed AA Osman, Siyu Tang, Chun-Hao P Huang, and Michael J Black. On self-contact and human pose. In *Proceedings of the IEEE/CVF Conference on Computer Vision and Pattern Recognition*, pages 9990–9999, 2021. 2
- [45] Evonne Ng, Donglai Xiang, Hanbyul Joo, and Kristen Grauman. You2me: Inferring body pose in egocentric video via first and second person interactions. In *Proceedings of the IEEE/CVF Conference on Computer Vision and Pattern Recognition*, pages 9890–9900, 2020. 3, 6
- [46] Tuomas Oikarinen, Daniel Hannah, and Sohrob Kazerounian. Graphmdn: Leveraging graph structure and deep learning to solve inverse problems. In *2021 International Joint Conference on Neural Networks (IJCNN)*, pages 1–9. IEEE, 2021. 2, 3
- [47] Mohamed Omran, Christoph Lassner, Gerard Pons-Moll, Peter Gehler, and Bernt Schiele. Neural body fitting: Unifying deep learning and model based human pose and shape estimation. In *2018 international conference on 3D vision (3DV)*, pages 484–494. IEEE, 2018. 2
- [48] Georgios Pavlakos, Vasileios Choutas, Nima Ghorbani, Timo Bolkart, Ahmed AA Osman, Dimitrios Tzionas, and Michael J Black. Expressive body capture: 3D hands, face, and body from a single image. In *Proceedings of the IEEE Conference on Computer Vision and Pattern Recognition*, pages 10975–10985, 2019. 1, 2
- [49] Georgios Pavlakos, Nikos Kolotouros, and Kostas Daniilidis. Texturepose: Supervising human mesh estimation with texture consistency. In *Proceedings of the IEEE/CVF International Conference on Computer Vision*, pages 803–812, 2019. 2
- [50] Paul-Edouard Sarlin, Mihai Dusmanu, Johannes L. Schönberger, Pablo Speciale, Lukas Gruber, Viktor Larsson, Ondrej Miksik, and Marc Pollefeys. LaMAR: Benchmarking Localization and Mapping for Augmented Reality. In *ECCV*, 2022. 2
- [51] Saurabh Sharma, Pavan Teja Varigonda, Prashast Bindal, Abhishek Sharma, and Arjun Jain. Monocular 3D human pose estimation by generation and ordinal ranking. In *Proceedings of the IEEE/CVF international conference on computer vision*, pages 2325–2334, 2019. 2, 3

- [52] Takaaki Shiratori, Hyun Soo Park, Leonid Sigal, Yaser Sheikh, and Jessica K Hodgins. Motion capture from body-mounted cameras. In *ACM SIGGRAPH 2011 papers*, pages 1–10. 2011. [3](#)
- [53] Jascha Sohl-Dickstein, Eric Weiss, Niru Maheswaranathan, and Surya Ganguli. Deep unsupervised learning using nonequilibrium thermodynamics. In *International Conference on Machine Learning*, pages 2256–2265. PMLR, 2015. [2](#), [3](#), [5](#)
- [54] Jie Song, Xu Chen, and Otmar Hilliges. Human body model fitting by learned gradient descent. 2020. [2](#)
- [55] Jiaming Song, Chenlin Meng, and Stefano Ermon. Denoising diffusion implicit models. *International Conference on Learning Representations, ICLR*, October 2021. [2](#), [3](#)
- [56] Yang Song, Jascha Sohl-Dickstein, Diederik P Kingma, Abhishek Kumar, Stefano Ermon, and Ben Poole. Score-based generative modeling through stochastic differential equations. In *International Conference on Learning Representations*, 2021. [2](#), [3](#), [5](#)
- [57] Omid Taheri, Nima Ghorbani, Michael J Black, and Dimitrios Tzionas. Grab: A dataset of whole-body human grasping of objects. In *Computer Vision—ECCV 2020: 16th European Conference, Glasgow, UK, August 23–28, 2020, Proceedings, Part IV 16*, pages 581–600. Springer, 2020. [2](#)
- [58] Jun Kai Vince Tan, Ignas Budvytis, and Roberto Cipolla. Indirect deep structured learning for 3D human body shape and pose prediction. 2017. [2](#)
- [59] Guy Tevet, Sigal Raab, Brian Gordon, Yonatan Shafir, Amit H Bermano, and Daniel Cohen-Or. Human motion diffusion model. *arXiv preprint arXiv:2209.14916*, 2022. [2](#), [3](#)
- [60] Denis Tome, Thiemo Alldieck, Patrick Peluse, Gerard Pons-Moll, Lourdes Agapito, Hernan Badino, and Fernando De la Torre. Selfpose: 3d egocentric pose estimation from a headset mounted camera. *arXiv preprint arXiv:2011.01519*, 2020. [3](#)
- [61] Denis Tome, Patrick Peluse, Lourdes Agapito, and Hernan Badino. xr-egopose: Egocentric 3d human pose from an hmd camera. In *Proceedings of the IEEE/CVF International Conference on Computer Vision*, pages 7728–7738, 2019. [3](#)
- [62] Jonathan Tseng, Rodrigo Castellon, and C Karen Liu. Edge: Editable dance generation from music. *arXiv preprint arXiv:2211.10658*, 2022. [3](#)
- [63] Timo von Marcard, Roberto Henschel, Michael J Black, Bodo Rosenhahn, and Gerard Pons-Moll. Recovering accurate 3d human pose in the wild using imus and a moving camera. In *Proceedings of the European Conference on Computer Vision (ECCV)*, pages 601–617, 2018. [6](#)
- [64] Tom Wehrbein, Marco Rudolph, Bodo Rosenhahn, and Bastian Wandt. Probabilistic monocular 3D human pose estimation with normalizing flows. In *Proceedings of the IEEE/CVF international conference on computer vision*, pages 11199–11208, 2021. [2](#), [3](#), [5](#)
- [65] Zhenzhen Weng and Serena Yeung. Holistic 3D human and scene mesh estimation from single view images. In *Proceedings of the IEEE/CVF Conference on Computer Vision and Pattern Recognition*, pages 334–343, 2021. [2](#)
- [66] Chen Xin, Biao Jiang, Wen Liu, Zilong Huang, Bin Fu, Tao Chen, Jingyi Yu, and Gang Yu. Executing your commands via motion diffusion in latent space. *arXiv*, 2022. [2](#), [3](#)
- [67] Hongyi Xu, Eduard Gabriel Bazavan, Andrei Zanfir, William T Freeman, Rahul Sukthankar, and Cristian Sminchisescu. Ghum & ghuml: Generative 3d human shape and articulated pose models. In *Proceedings of the IEEE/CVF Conference on Computer Vision and Pattern Recognition*, pages 6184–6193, 2020. [2](#)
- [68] Yuanlu Xu, Song-Chun Zhu, and Tony Tung. Denserac: Joint 3D pose and shape estimation by dense render-and-compare. In *Proceedings of the IEEE/CVF International Conference on Computer Vision*, pages 7760–7770, 2019. [2](#)
- [69] Vickie Ye, Georgios Pavlakos, Jitendra Malik, and Angjoo Kanazawa. Decoupling human and camera motion from videos in the wild. *arXiv preprint arXiv:2302.12827*, 2023. [3](#)
- [70] Ye Yuan and Kris Kitani. Ego-pose estimation and forecasting as real-time pd control. In *Proceedings of the IEEE/CVF International Conference on Computer Vision*, pages 10082–10092, 2019. [3](#)
- [71] Ye Yuan, Jiaming Song, Umar Iqbal, Arash Vahdat, and Jan Kautz. Physdiff: Physics-guided human motion diffusion model. *arXiv preprint arXiv:2212.02500*, 2022. [3](#)
- [72] Jianfeng Zhang, Dongdong Yu, Jun Hao Liew, Xuecheng Nie, and Jiashi Feng. Body meshes as points. In *Proceedings of the IEEE/CVF Conference on Computer Vision and Pattern Recognition*, pages 546–556, 2021. [2](#)
- [73] Mingyuan Zhang, Zhongang Cai, Liang Pan, Fangzhou Hong, Xinying Guo, Lei Yang, and Ziwei Liu. Motiondiffuse: Text-driven human motion generation with diffusion model. *arXiv preprint arXiv:2208.15001*, 2022. [2](#), [3](#)
- [74] Siwei Zhang, Qianli Ma, Yan Zhang, Zhiyin Qian, Taein Kwon, Marc Pollefeys, Federica Bogo, and Siyu Tang. Ego-body: Human body shape and motion of interacting people from head-mounted devices. In *Computer Vision—ECCV 2022: 17th European Conference, Tel Aviv, Israel, October 23–27, 2022, Proceedings, Part VI*, pages 180–200. Springer, 2022. [1](#), [6](#)
- [75] Yi Zhou, Connelly Barnes, Lu Jingwan, Yang Jimei, and Li Hao. On the continuity of rotation representations in neural networks. In *The IEEE Conference on Computer Vision and Pattern Recognition (CVPR)*, June 2019. [1](#)
- [76] Yuxiao Zhou, Marc Habermann, Ikhsanul Habibie, Ayush Tewari, Christian Theobalt, and Feng Xu. Monocular real-time full body capture with inter-part correlations. In *Proceedings of the IEEE/CVF Conference on Computer Vision and Pattern Recognition*, pages 4811–4822, 2021. [2](#)
- [77] Zhiming Zou and Wei Tang. Modulated graph convolutional network for 3d human pose estimation. In *Proceedings of the IEEE/CVF International Conference on Computer Vision*, pages 11477–11487, 2021. [2](#), [5](#), [1](#)

Probabilistic Human Mesh Recovery in 3D Scenes from Egocentric Views

Appendix

A. Architecture Details

The detailed model architecture is illustrated in Fig. S1. The local scene encoder E_S is an MLP network consisting of several residual blocks to encode the cropped input scene point cloud of M points (translated by the estimated body translation $\hat{\gamma}$ from the camera coordinate system) into a 512-d scene feature. In the diffusion denoiser D , for each joint j , we use the 6D representation [75] to represent the joint rotations. A linear layer first maps the input noisy pose parameters θ_t^j into a 512-d pose embedding. The timestep t is embedded by an MLP with the sinusoidal function. The pose embedding is concatenated with the corresponding context embedding (including the image feature, scene feature, timestep embedding, \mathcal{B} , \mathcal{K} , and the estimated body translation $\hat{\gamma}$) as the input feature for node j in the GCN. The GCN module consists of an input GCN layer, followed by four residual modulated GCN blocks [77] and a final GCN layer, which outputs the clean pose parameters $\hat{\theta}_0^j$ for each joint j .

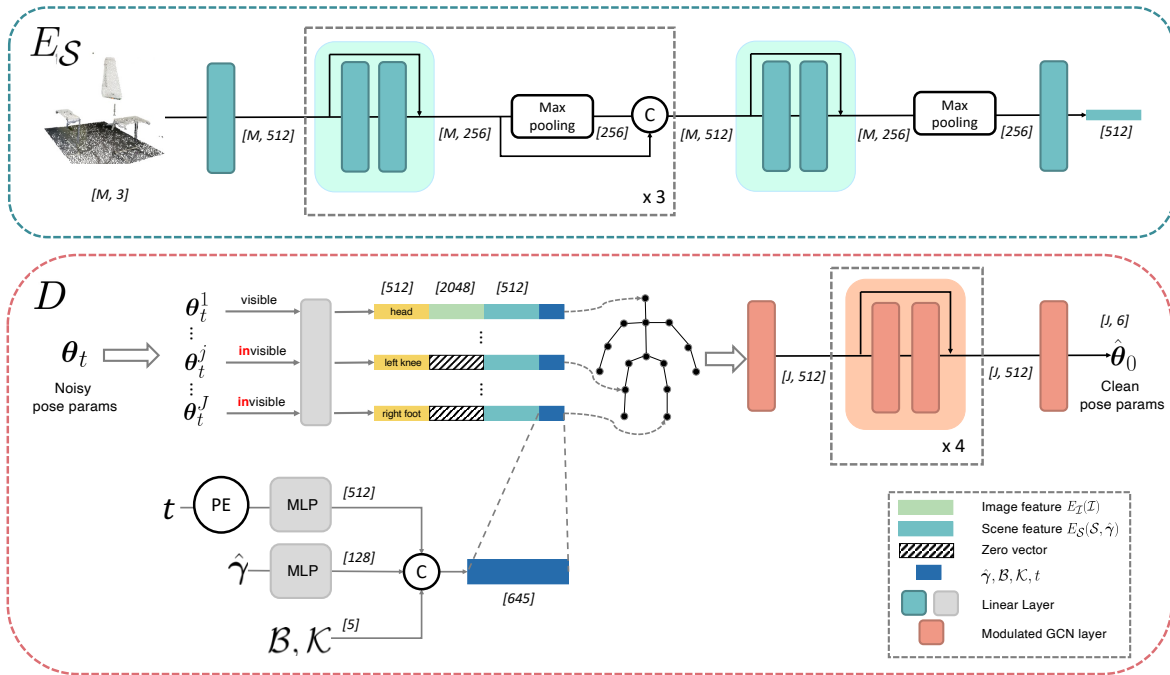


Figure S1: **Architecture details for the local scene encoder E_S and the diffusion denoiser D .** Numbers in '['] indicates the corresponding feature dimension. PE stands for positional encoding.

B. Body Translation Estimator

As the body translation is coupled with the body shape and pose parameters in the SMPL model, an accurate estimation of γ also relies heavily on the learning of the body pose θ and shape β . We adopt ProHMR [30] as the backbone for the body translation estimator, which estimates (γ, θ, β) jointly, but with three major modifications.

First, the scale ambiguity between γ and β poses great challenges to the accurate global translation prediction in [30] with a single image as the input. We leverage the 3D scene point cloud S with a global scene encoder to extract the global scene feature. The global scene encoder has the same architecture as the local scene encoder in Fig. S1, but with the full scene point cloud S in the camera coordinate system as the input. The encoded global scene feature is concatenated with the

image feature (encoded by a ResNet50 backbone [14]) as the conditioning input to the normalizing flow. Second, existing works [22, 25, 30] take the cropped image (containing the target person, resized to a fixed resolution) as the input, which discards the location information in the full image camera coordinate system. The ignorance of the original camera introduces additional ambiguity and results in inaccurate estimations of global information. Besides the cropped image features, we additionally feed the bounding box information \mathcal{B} in Eq. (4) to the network to provide global-aware features. On top of that, the predicted body is transformed back to the original camera coordinate system and the 2D keypoint reprojection loss is calculated in the full image instead of the cropped image. The projected 2D keypoints in the original image have similar perspective distortions with the person in the full image, offering better supervision for 3D predictions [34]. Last but not least, the model is further conditioned on the camera intrinsics \mathcal{K} such that it can be adapted to different cameras and headsets.

Here the supervision on body pose θ and body shape β provides auxiliary information for the accurate estimation of the body translation. And we employ this straightforward scene-conditioned model as the baseline method ProHMR-scene (Sec. 5.3). However, the 3D scene features here are not sufficiently localized to learn fine-grained human-scene interactions for local body pose (as demonstrated in Sec. 5.4), thus we only take the predicted translation $\hat{\gamma}$ from this model, and propose the scene-conditioned pose diffusion model for better local pose reasoning.

To train the body translation estimator we employ the same training objectives as in [30], but with the 2D keypoint re-projection loss calculated in the full image frame. The trained model also serves as the ProHMR-scene-orig baseline (Sec. 5.3).

C. Experiment Details

C.1. Implementation Details

Training details. The image encoder $E_{\mathcal{I}}(\mathcal{I})$ is loaded from the pretrained weights from [30] (for our method and all baseline methods). For the ProHMR baseline, we load the entire pretrained checkpoint from [30] and fine-tune it on EgoBody dataset. In our model, the body translation estimator and the local pose diffusion model are trained separately. The diffusion model is trained with the ground truth body translation γ . During inference, we use the predicted $\hat{\gamma}$ from the body translation estimator to crop and translate the local scene point cloud to encode the local scene feature, and feed $\hat{\gamma}$ as the input to the diffusion model. The body pose θ is transformed from the 6D representation to the rotation matrix to calculate $\mathcal{L}_{\text{simple}}$. The weights for $\mathcal{L}_{\text{simple}}$, \mathcal{L}_{3D} , \mathcal{L}_{2D} , \mathcal{L}_{β} , $\mathcal{L}_{\text{coll}}$, $\mathcal{L}_{\text{orth}}$ are 0.001, 0.05, 0.01, 0.0005, 0.0002, and 0.1, respectively. The collision loss term $\mathcal{L}_{\text{coll}}$ is disabled for the first three epochs. The model is trained with a single TITAN RTX GPU of 24GB memory for approximately 18 epochs, with a batch size of 12, which takes around 24 hours.

Collision score guided sampling. In Eq. (9), we set a as 2. For the last 10 diffusion denoising timesteps, we ignore the Σ_t and only scale $\nabla \mathcal{J}(\theta_t), \Sigma_t$ by a such that the collision score guidance does not diminish too much at the end of the sampling process.

Evaluation protocol. For the evaluation, the standard PA-alignment is obtained from the full body joints, however in the highly truncated case the diverse nature of invisible body parts could deviate from the ground truth and result in inaccurate PA-alignment, thus we perform PA-alignment with only visible body joints and report the PA-MPJPE metric.

C.2. Ablation Study on Model Architecture and Per-joint Conditioning

We also conduct experiments with the following two architectures as the diffusion denoiser D to verify the effectiveness of our proposed per-joint visibility conditioning strategy and the GCN architecture: (1) a single MLP network to predict the full body pose conditioned on $c = (E_{\mathcal{I}}(\mathcal{I}), E_{\mathcal{S}}(\mathcal{S}, \hat{\gamma}), \hat{\gamma}, \mathcal{B}, \mathcal{K}, t)$, *i.e.* the image feature, the scene feature, the bounding box information, the camera intrinsics and the diffusion timestep, without the per-joint visibility mask, denoted as ‘full-body MLP’; (2) using the same per-joint conditioning strategy as our proposed method, but with J MLP networks to predict the pose parameters for each body joint separately, where the MLPs share the same architecture but with different weights, denoted as ‘per-joint MLP’. The results are shown in Tab. S1.

For the per-joint MLP model, there is a significant drop on sample diversity for invisible body parts, as such model architecture disables the classifier-free guidance. With the classifier-free guidance, the pose for invisible body parts sampled from the model excluding the image condition can be fused into the standard sampling results, thus improving the sample diversity for invisible body parts. With a separate MLP for each body joint independently from other joints, each MLP for the invisible joint already excludes the image condition, therefore no additional classifier-free guidance can be applied on top of that to further improve diversity. Different from the GCN architecture which considers the human kinematic tree, the per-joint MLP model neglects the inter-joint dependencies, which are crucial to model human poses and human-scene interactions. Due to this reason, the *min-of-n* MPJPE for invisible joints of the per-joint MLP model is also higher compared

Table S1: **Ablation study for model design choices.** All experiments are conducted without the scene collision score guidance $\mathcal{J}(\theta_t)$. The results are reported for $n = 5$.

Method	MPJPE ↓ -vis	<i>min-of-n</i> MPJPE ↓ -invis	coll ↓	contact ↑	std ↑ -invis	APD ↑ -invis
Ours	65.10	107.59	0.00225	0.99	20.30	25.34
Per-joint MLP	65.35	113.62	0.00225	0.99	16.50	20.51
Full-body MLP	65.65	111.67	0.00228	0.98	11.08	12.98



Figure S2: **More qualitative examples.** For both left and right sides: (a) the input egocentric image; (b) the rendered body mesh overlay on the input image; (c) the rendered body mesh in the 3D scene.

to the proposed GCN architecture, indicating that the generated body pose for visible body parts cannot cover the ground truth distribution well enough.

For the full-body MLP model, the full body pose is conditioned on the image and scene feature. Without the explicit per-joint visibility information, the network can hardly achieve the precise per-body-part control, therefore struggling to balance between the accuracy and diversity for different body parts (with the lowest diversity compared with other two models in Tab. S1). On the contrary, our proposed per-joint conditioning strategy can leverage the joint visibility to achieve both accuracy for visible joints and diversity for invisible joints, together with plausible human-scene interactions.

D. More Qualitative Results

More qualitative examples and diverse sampling results of our proposed method are shown in Fig. S2 and Fig. S3, respectively. While obtaining accurate pose estimations aligning with the input image, our method also achieves impressive sample diversity for the unobserved body parts, with plausible human-scene interaction relationships.

E. Limitations and Future Work

Apart from the static human pose, human motions also play an important role in human behavior understanding from the egocentric view. One of the limitations of the proposed method is that it only allows per-frame human mesh recovery given a single frame input. Human motion estimation from an egocentric temporal sequence in 3D scenes would be an exciting future work and enable more real-life AR/VR applications. Besides, the current model relies on a two-stage pipeline, which

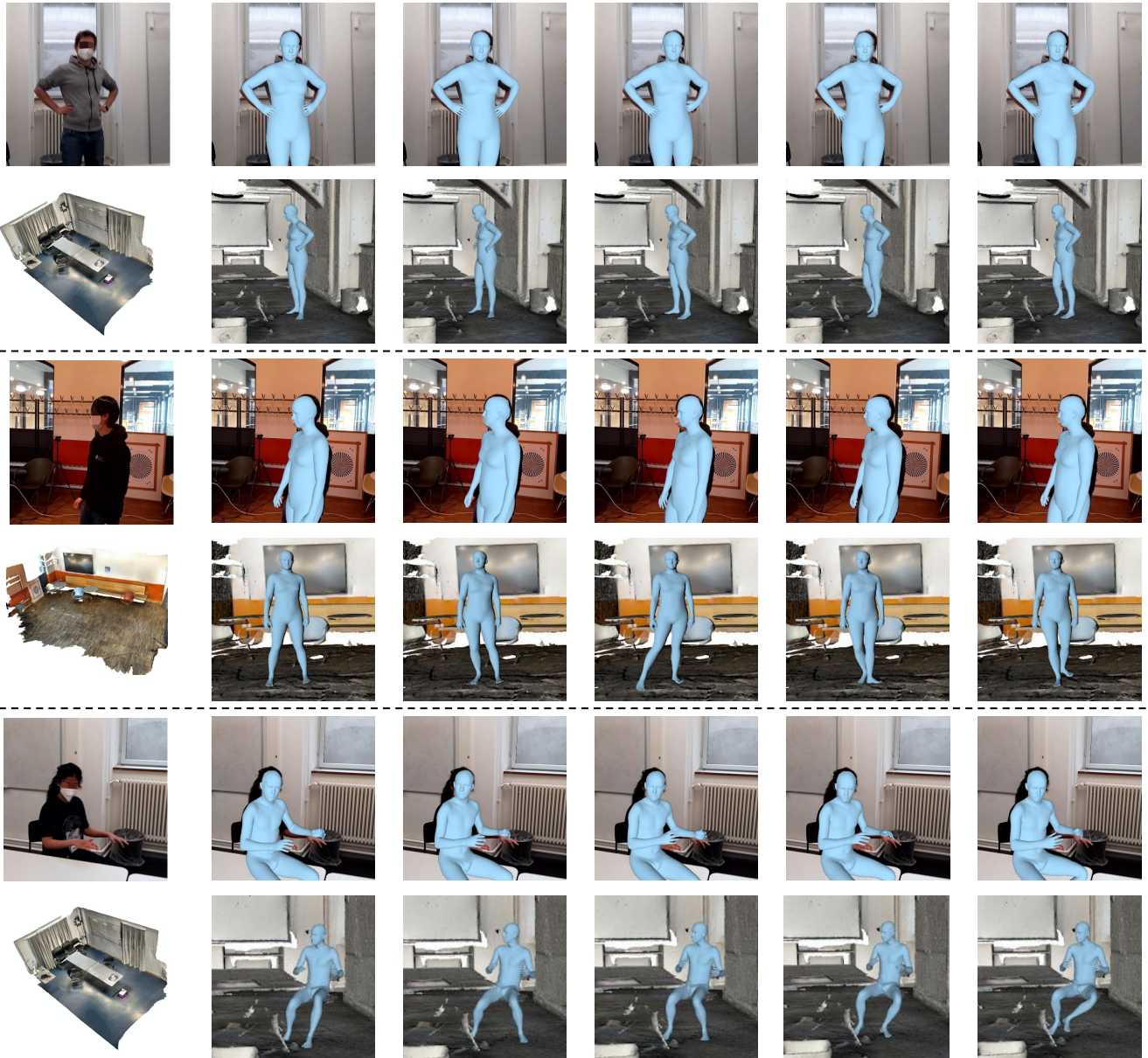


Figure S3: **More examples for diverse sampling.** Each row shows five different sample results given the input image and 3D environment (the first column).

estimates the global body translation and local body pose in separate stages. However, the global translation, local body pose and body shape are coupled together, and equally important for learning the interactions between the human body and the 3D environment. A unified end-to-end model to learn the body parameters altogether would be desired and potentially provide better reasoning about human-scene interaction relationships.